JOURNAL OF PROPULSION AND POWER
Vol. 25, No. 6, November–December 2009

Single-Phase Internal Flowfield Validation with an Experimental Solid Rocket Motor Model

B. Tóth,* M. R. Lema,† P. Rambaud,‡ and J. Anthoine§
von Karman Institute for Fluid Dynamics, 1640 Rhode-Saint-Genèse, Belgium
and
J. Steelant¶
ESA, 2200 AG Noordwijk, The Netherlands

DOI: 10.2514/1.42453

Incorporating a submerged nozzle for solid propellant rocket motors, the resulting cavity formed in the vicinity of the nozzle integration part enhances the entrapment of liquid residues of the combustion and leads to the accumulation of slag with a considerable mass. As a first step for the slag accumulation assessment, an experimental and numerical investigation of the single-phase internal flowfield is performed and the numerical tool is validated. The measurements are carried out in a cold-gas simplified model in which the flow is injected from the forward end (no wall injection). Simultaneously, the experimental configuration is simulated numerically with the help of a commercial solver (CFD-ACE+). The experimental results allowed the full characterization of the complex recirculation zone downstream of the inhibitor model and in the cavity. It was also demonstrated that the airflow in the cavity is slightly altered in case the gas–slag interface is represented either as a rigid or a liquid. The time-averaged statistical results of the three-dimensional simulation in the midspan plane compare very well to the experimental database, ensuring a satisfactory validation. The mean streamlines close to the walls, plotted from the computational fluid dynamics field, allow better understanding of the flow structures. The analysis reveals a two-dimensional flowfield for the studied geometry with locally some three-dimensional behaviors, especially along the main recirculation bubble interface.

Nomenclature

H = height of the channel
h = height of the inhibitor
Re_h = Reynolds number based on h
rms_U = root mean square of the U velocity component
rms_V = root mean square of the V velocity component
rms_W = root mean square of the W velocity component
U = streamwise velocity component
U_0 = freestream velocity
V = transversal velocity component
W = out-of-plane velocity component
x, y, z = Cartesian body axes
Δt = particle image velocimetry separation time

Introduction

THE first stage of launch vehicles (e.g., Ariane 5, Vega, Shuttle, Ares, H-II) generally incorporates solid propellant rocket motors (SRM). These are typically operating during the first part of the liftoff, providing most of the thrust to accelerate the vehicle. To shorten the overall length, the nozzle is submerged in the last segment of solid propellant. That means that the convergent, the sonic throat, and part of the divergent are surrounded by solid propellant. This integration allows orientation of the nozzle to provide adaptation of the rocket trajectory during the launch. During the combustion (please see Fig. 1), the regression of the solid propellant surrounding the nozzle integration part leads to the formation of a cavity around the nozzle lip. The aluminum, being part of the propellant grain composition, is oxidized during the combustion. This process goes along with the generation of alumina droplets, which are then carried by the hot core flow toward the nozzle. Meanwhile, the droplets interact with the vortices formed by the internal flow and thus may modify their structure. As a consequence, some of the droplets are entrapped in the cavity instead of being exhausted through the throat. The amount of entrapped droplets in the cavity depends most probably on their interaction with the vortices. The accumulation of these droplets in the cavity generates an alumina puddle, also called slag. This slag reduces the performance of the solid propellant motor due to its dead weight and absence of impulse generation. In the case of the Ariane 5 solid rocket motors (MPS P230) the total mass of the accumulated particles can reach up to 2 tons in each motor by the end of the launch [1].

Background and Objectives

The present section describes the previous works carried out to assess the problem and the objectives of the current investigation.

Previous Studies Related to Slag Accumulation

Slag accumulation in aluminized SRMs has already been studied directly or indirectly through numerous projects pointing out various consecutive mechanisms driving the entrapment of alumina droplets. The first obvious steps in this process are the aluminum combustion, the alumina formation, and the generated droplet size distribution, which have been studied by several authors [2–5].

The entrainment and transport once the droplets are flowborne have been investigated first through quasi-steady numerical simulations [6–8]. However, the unsteady nature of the internal flowfield has proven to be important [9,10]. Also, the slag accumulation was

---

Received 28 November 2008; revision received 31 May 2009; accepted for publication 22 June 2009.

*Postdoctoral Candidate, Environmental and Applied Fluid Dynamics Department, Chaussée de Waterloo 72; balazst@gmail.com. Student Member AIAA.

†Research Engineer, Environmental and Applied Fluid Dynamics Department, Chaussée de Waterloo 72.

‡Assistant Professor, Environmental and Applied Fluid Dynamics Department, Chaussée de Waterloo 72.

§Associate Professor, Environmental and Applied Fluid Dynamics Department, Chaussée de Waterloo 72. Member AIAA.

¶Senior Researcher, European Space Research and Technology Centre, Technical and Quality Management Directorate, Aerothermodynamics and Propulsion Analysis Section, Keplerlaan 1, P.O. Box 299; Johan.Steelant@esa.int. Member AIAA.

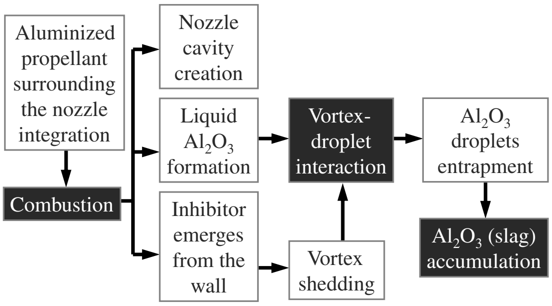

Fig. 1 Topology of the problem.

shown to be linked to the pressure oscillations occurring in the SRMs [10,11]. As these oscillations are related to different internal vortex generation mechanisms, several studies were dedicated to assess these processes [12–14]. Furthermore, the interaction of the droplets with the internal surfaces of the motor and the behavior of the eventually formed liquid film (primarily on the nozzle lip) have been addressed [15,16] to evaluate whether a droplet contributes to the slag or returns to the flow.

Finally, once the slag is deposited in the cavity, its negative contribution to the launch does not finish. Being liquid, it can slosh inside the cavity [17]. Further, if the aerodynamic forces are strong enough (and/or combined with the sloshing), slag may be ejected through the nozzle. Though the onboard dead mass decreases, the momentum impulse loss of the motor cannot be recovered. Furthermore, depending on the amount of ejected slag, thrust oscillations may occur leading to control problems and possible vehicle instabilities [18]. Another consequence of the slag ejection is that the total amount of the actually accumulated alumina might be higher than what is observed after a firing test or launch.

In spite of many (predominantly) numerical investigations of the slag accumulation and the internal flow in SRMs [19–22], the occurring processes are still not fully understood. There is no known model that could entirely describe the accumulation mechanism and provide clear suggestions to designers to minimize the slag mass in future launchers. In addition, the available experimental observations are even more limited and, in the case of a real motor, they are mostly limited to global accumulated slag mass [19] or internal pressure evolutions [23]. The lack of a more detailed experimental database, including the quantification of the interaction between the two phases, limits the validation and application of the numerical models.

Objectives

There is a clear need for a more fundamental study of the vortex–droplet interaction, the slag accumulation process, and the generation of a detailed experimental database for numerical validation. To achieve this goal, the driving parameters of the slag accumulation are characterized in a simplified 2-D-like cold-gas model [24]. The interaction of droplets with the flow and the entrapment process of the droplets in a stagnant area modeling the nozzle cavity are investigated primarily experimentally. However, not only a detailed experimental database is produced, but numerical simulations are also performed and validated to explore its limitations and strengths.

The importance of the unsteady nature of the internal flowfield dictates the first requirement being the quantification of the main internal flowfield features. Therefore, a single-phase particle image velocimetry (PIV) measurement campaign was set up for the cold-gas model without droplets to understand that single-phase flow behavior. These experiments form a solid validation database for the three-dimensional large-eddy simulation (LES) involved in the prediction of the single-phase flow. The present paper focuses on this first requirement. Once successfully validated, the numerical tool will populate a vast database providing further insight in the flow topology. Afterward, the tool should be applied, expecting to understand the liquid accumulation process.

Previous Works on Single-Phase Flow Investigation in Solid Rocket Motors

Cold-gas experimental setups were developed to analyze primarily potential unstable mechanisms in the internal flowfield of SRMs. The reason for operating these facilities with cold gasses remains in their low operating cost and because combustion is believed to take a minor part in the instability mechanism. Cold flow experiments in a pipe with one or two inhibitors were conducted, for example, by Culick and Magiawala [25], Dunlap and Brown [26], Mettenleiter et al. [27], and Anthoine et al. [28]. Other cold-gas facilities have been developed within the Aerodynamics of Segmented Solid Motors program, focusing mainly on the hydrodynamic instability, which appears in the Ariane 5 MPS [29]. Some of these facilities have been used more recently by Vetel et al. [30] investigating the influence of the inhibitor shape, and by Nguyen et al. [31] analyzing the effect of the injecting wall inclination. Anthoine and Lema [32] determined the performance of passive control systems to reduce the pressure oscillations through cold-gas experiments.

Because the primary goal of all these cold-gas setups is to analyze the unstable mechanism of flow-acoustic coupling, the resulting experimental database consists of unsteady pressure, mainly at the forward end, and a few velocity fluctuation profiles. The latter are obtained using either hot-wire anemometry or laser Doppler velocimetry. To obtain a database that characterizes the unsteady internal flowfield of the complete facility, the most promising technique is the particle image velocimetry. The PIV is a nonintrusive measurement technique that provides instantaneous velocity vector fields [33]. Because most of the PIV systems commonly used do not provide flowfields resolved in time, the technique is not suitable for flow-acoustic investigation. This explains why it has been scarcely applied to cold-gas facilities up until now. Anthoine et al. [34] used it, for example, for the assessment of an adaptive control system and not for generating a database for numerical validation.

For the numerical simulation of a turbulent flow in an industrial configuration, the direct numerical simulation is usually not suitable because of its prohibitive CPU cost. Instead, generally, a mathematical modelization is used to predict the effect of the most distinguishing features due to turbulence [35]. The main alternatives are the Reynolds-averaged Navier–Stokes (RANS) model aiming for a convergence toward a steady solution, and the LES model aiming for a range of instantaneous flow solutions.

The RANS approach is widely used to solve engineering-type problems. However, the obtained time-averaged solution may be unable to reproduce some details of the physics [36] due to the lack of universality upon which the proposed turbulence models are built.

The LES approach offers a time-dependent set of solutions. Formally, the set of LES equations to be solved is obtained by a methodology similar to the one used for RANS. In LES, the contribution of the large energy carrying structures is computed exactly (i.e., resolved), and only the effect of the smallest scales of turbulence is modeled by using the so-called subgrid-scale model (SGS) such as the one proposed by Smagorinsky [37]. Because the small scales are hypothetically homogeneous and isotropic, and less affected by the boundary conditions than the large ones, the SGS models are mostly simpler in nature. Nevertheless, they constantly require an adjustment when applied to different flows. To lower this dependence to an arbitrary constant (often labeled Cs), a dynamic model had been proposed by Germano et al. [38]. Several contributions have attempted to compare the dynamic and Smagorinsky SGS models for the LES [39–41]. The dynamic model generally gives a better agreement with the experiments without the difficult determination of a prescribed value.

A fine spatial and temporal description of the vorticity is a next step to properly determine the amount of droplets entrained in the cavity by the vortices. It is believed that the LES technique with dynamic modeling of the SGS terms is a more appropriate description and probably outperforms the unsteady RANS or Detached Eddy Simulation techniques [42]. Of course, at the present step, the price to pay to obtain only a time-averaged solution is considerably higher in CPUs than an equivalent RANS simulation, keeping in mind that wall-resolved LES often requires a fairly fine mesh. However, if this choice proves to lead to an accurate representation of the time average made over a larger set of instantaneous solutions, then this set will be directly applicable for studying the particle–vortex interactions. The higher cost is then thought acceptable.

Numerical simulations were used to highlight the hydrodynamic instabilities and their coupling with the acoustics [12,43–47]. More recently, the LES approach has been applied to simulate the unsteady flow evolution in porous chambers by Apte and Yang [48–50], Vetel et al. [51], and Plourde et al. [52].

Experimental Conditions

The geometry of the experimental model (see Fig. 2) simulates the main characteristic features of the MPS P230. The square ($200\times 200\ \mathrm{mm}^2$) test section has a symmetric arrangement. In reality, in the axisymmetric SRM, vortex rings are shed from a ring-shaped inhibitor. In a 2-D-like configuration having two symmetrically placed inhibitors, an interaction could occur between the vortex shedding from both sides. As a result, the vortex generation at the two inhibitors could result in a 180 deg shift. To prevent this coupling, a 5-mm-thick splitting plate divides the two sides of the test section. Because the square test section has a symmetric arrangement and therefore a symmetric flow condition, the measurements are carried out by using only one side of the test section.

The height of the inhibitor is $h = 33.5$ mm. The presence of this fence induces the obstacle vortex shedding. To allow the vortices to reach the nozzle and reproduce the vortex–nozzle interaction phenomenon in the 2-D model, the inhibitor is placed at $L_i = 9h$ from the nozzle.

At the bottom of the cavity, a 30-mm-thick Plexiglas piece models the accumulated liquid. Later, the Plexiglas piece is replaced by the same amount of water to see the importance of a liquid interface with respect to the solid wall.

The current single-phase experiments are carried out at room temperature using air to model the internal fluid of the SRM. A freestream velocity of $U_0 = 10\ \mathrm{m/s}$ is chosen, which results in $Re_h = 2.51\times 10^4$. In comparison, for MPS P230 this parameter exceeds $Re_h > 10^6$. Nevertheless, by respecting the turbulent flow regime, the viscous effects remain similarly negligible. Furthermore, the chosen velocity corresponds to a Mach number of about $M = 0.03$, which is on the order of $M = 0.1$ in the real motor just upstream the convergent part of the nozzle. In the cold-gas model, due to the construction of the setup, the sonic condition at the nozzle throat is not respected.

In Fig. 2, the setup is shown in its real (vertical) orientation. However, later, the geometry will always be represented horizontally. The test section (depicted in Fig. 2b) is designed in a way to allow the use of optical measurement techniques (e.g., PIV) to characterize the internal flowfield. Therefore, most of the walls are made of transparent material.

To characterize the single-phase internal flowfield of the 2-D-like simplified model of the SRM, the PIV technique is used [33].

The laser sheet representing the measurement plane is generated in the midspan plane of the test section, perpendicular to the splitting plate. The tracers are oil particles on the order of 1–2 μm in diameter. A camera with $1280\times 864\ \mathrm{pixels}^2$ effective resolution (placed perpendicular to the laser sheet) records the measurement image pairs.

Currently, the region of interest covers the whole midspan plane of the test section from the inhibitor to the nozzle throat, including the cavity. All this area should be investigated by the PIV experiments to be able to compare the data to numerical simulations. Furthermore, these measurements should have high enough resolution for validation purposes. Hence, the magnification of the images is limited to about 0.081 mm/pixel between the inhibitor and the nozzle and about 0.09 mm/pixel inside the cavity. The low magnification has a good contribution to the measurement quality near the walls of the section; this reduces the area of regions affected by the light reflections.

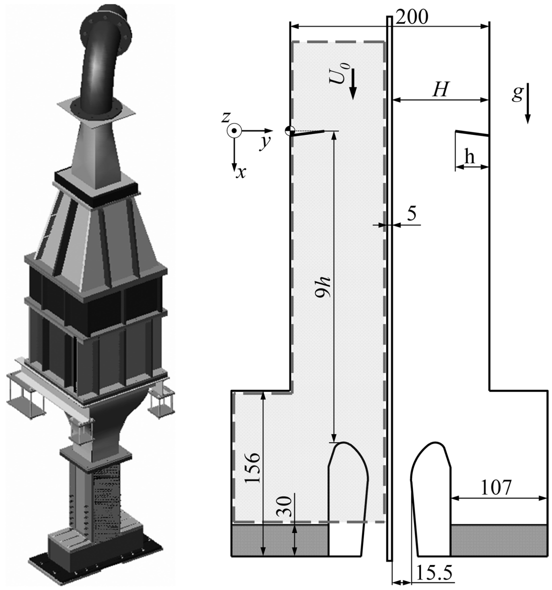

a) Wind tunnel **b) Test section**

Fig. 2 Experimental configuration.

To achieve the required higher spatial resolution, the region of interest is divided into 12 fields of view, which means that the measurement is performed by using 12 different camera positions (indicated in Fig. 3) one after the other. After the PIV analysis, once the mean flowfield of each FoV is computed, the 12 fields have to be combined to retrieve the mean flowfield of the whole region of interest. Therefore, special care of the spatial calibration (position and magnification) has to be taken. The 13th FoV shown in Fig. 3 covers the whole cavity. However, this field is not taken into account in the combined view.

Furthermore, special care is taken to achieve the highest possible overall signal-to-noise ratio (SN). Focusing on the region of the expected path of the vortices, the settings are tuned until the SN reaches mostly above four.

The separation time Δt between the PIV images is optimized in each FoV according to the actual magnification and the local flow conditions. In each FoV, 1000 image pairs are recorded, which allows to determine reliable turbulence quantities besides the mean velocity vectors. As mentioned before, all the plots of the different fields of view are combined and presented as one single field.

Experimental Results

During the PIV processing of each FoV (by using WiDIM, the PIV algorithm developed by Scarano [53,54]), the optimal initial window size and the number of window refinement iterations are determined according to the actual image quality. The switched-on window-distortion algorithm and the 75% window overlapping are common parameters of the data processing. As a result, for example, in the region between the inhibitor and the nozzle, the resolution of the velocity field is 1.4–2.5 vectors/mm by keeping a high mean SN (see Fig. 4).

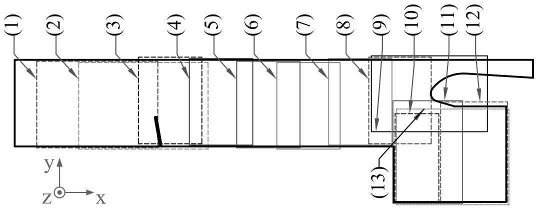

Fig. 3 Fields of view of the PIV measurements (the fields are slightly shifted transversely to facilitate understanding).

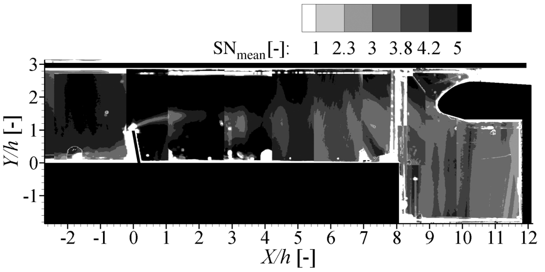

Fig. 4 Signal-to-noise ratio distribution of the PIV measurements.

While the statistical quantities are computed from the instantaneous flowfields, a validation process is carried out in every cell of each field. Where SN_{mean} does not reach a value of 2.3, the measurement is considered to be unacceptable. An indicator of this effect is, for example, when streamlines enter the wall. In the contour plots, these ambiguous areas appear in white (without value, see Fig. 4), which highlights that locally the measurement quality is low and the mean velocity vectors may not represent physical behavior.

Statistical Flow Quantities

During the analysis of the obtained statistical flow structures, the plane of interest and the boundaries are divided into several zones. The most frequently used terms are summarized in Fig. 5.

After combining the 12 fields of view recorded in the symmetry plane of the test section, at first the streamlines of the mean flow are shown in Fig. 6a. It can be observed that, in the mean, a flow particle, following the streamline which originates roughly from the tip of the inhibitor ($X/h = 0$, $Y/h = 1$), arrives at the nozzle head and escapes from the model through the throat. The flow particles placed at higher Y/h positions than this streamline directly escape as well.

As no radial flow injection occurs perpendicular to the side wall, a complex recirculation zone can be seen below this streamline (at lower Y/h values). This area is governed mainly by two mean rotating structures. One of them is located in the cavity, centered at ($X/h = 9.82$, $Y/h = -0.11$), and the other one extends from the tip of the inhibitor until the entrance of the cavity; its center is at ($X/h = 4.04$, $Y/h = 0.89$). At the downstream corner of the inhibitor and just upstream from the entrance of the cavity, smaller counter-rotating mean structures are formed. Because of local light reflection and image quality problems, the counter-rotating mean structures at the upstream corner of the inhibitor and in the three corners of the cavity could not be captured properly.

In the contour of Fig. 6b, the mean in-plane velocity magnitudes can be seen. It can be observed that the flow is accelerating as it passes over the inhibitor. The magnitude of the velocity reaches slightly above 21 m/s in the vena contracta. Then, the freestream flow slows down below 20 m/s. As it approaches the nozzle, it accelerates again and, in the nozzle throat, it reaches a velocity magnitude higher than 50 m/s. Unfortunately, this latter value could not be captured more precisely.

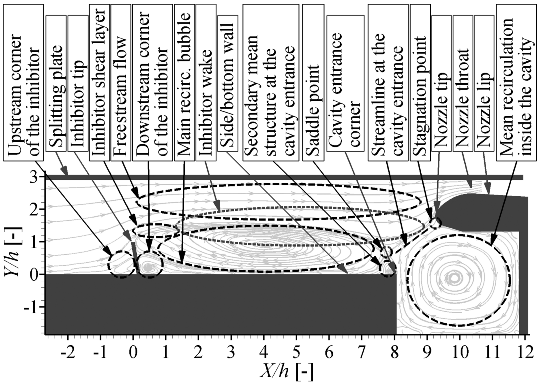

Fig. 5 Schematic of the main boundary elements and mean flow structures.

Considering the fluctuations, Figs. 6c and 6d show the rms of the streamwise U and of the transversal V velocity components, respectively. At the tip of the inhibitor, rms_U increases abruptly above 3.6 m/s due to the presence of a shear layer at the separation. The area from the inhibitor to the nozzle head may be divided roughly into two zones. In the first one, from $X/h = 0$ to $X/h = 4.2$ (corresponding approximately to the center of the main recirculation structure), the value of this fluctuation component is increasing and the contour of high values spreads gradually, reaching a value of about 50% of the initial freestream velocity U_0. In the second zone, from the center of the recirculation region to the nozzle head, the isocontours of this fluctuation component keep a constant width together with a constant maximum value of rms_U at about 50% of U_0.

The fluctuation of the transversal velocity component rms_V shows a similar evolution to rms_U, with a maximum value above 35% of U_0. However, in the second region, in front of the nozzle head, one may notice values above 45% of U_0, due to the local acceleration of the flow and turbulence production by the flow impingement on the nozzle wall.

In practice, the main fluctuations are driven by the shear layer attached to the inhibitor tip. Close to the inhibitor tip, the shear layer is very stable, representing mainly longitudinal fluctuation. Therefore, in a narrowband high rms_U values appear immediately.

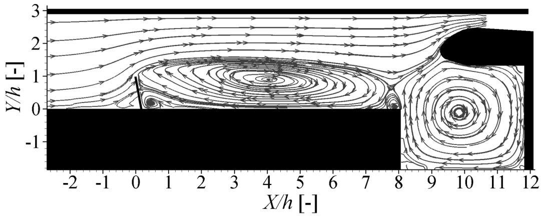

a) Streamlines of the mean flowfield

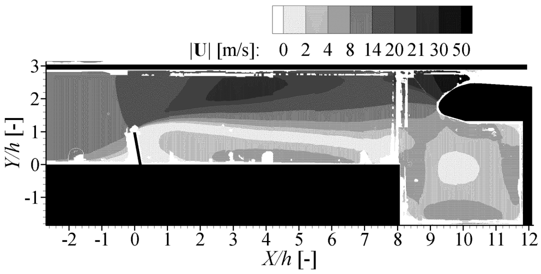

b) Mean velocity magnitude distribution

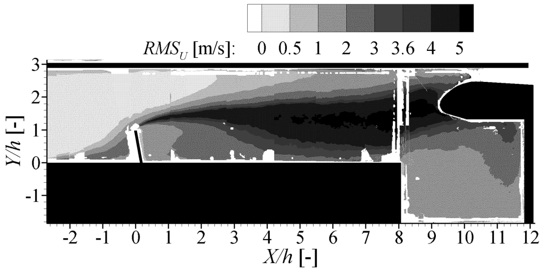

c) Fluctuation of the longitudinal velocity component

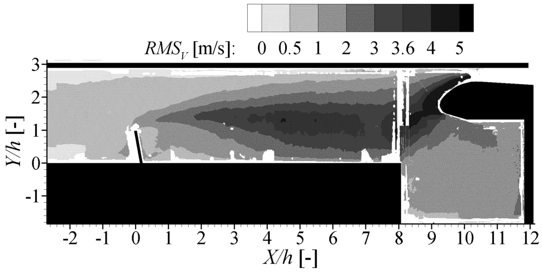

d) Fluctuation of the transversal velocity component

Fig. 6 Results of the ensemble-averaged PIV campaign in the symmetry plane.

However, shortly after the inhibitor, the shear layer starts flapping and breaks up into vortices, which make the transversal fluctuations rms_V increase gradually.

At the nozzle tip, depending on the vortex–nozzle interaction, vortical structures may enter the circulation zone inside the cavity [28]. Thus, in the cavity, they initiate the fluctuations. However, they probably dissipate and therefore, by the time the flow makes a 270 deg turn and arrives back to the entrance of the cavity, the fluctuations decay (also visible in Figs. 6c and 6d).

Effect of Slag in the Cavity

The statistical flow quantities are obtained by performing the experiments, while a 30-mm-thick Plexiglas sheet is placed in the cavity, which models the accumulated liquid. In the present section, the influence of the rigid surface with respect to the deformable liquid interface is assessed. Therefore, 30 mm of water is poured into the cavities and the mean flow topology is investigated using one FoV.

The comparison of the two cases can be seen in Fig. 7. Because of the presence of waves, high-energy laser light reflections occur above the water surface. To protect the camera from dangerous reflections, the interface area is not characterized (white region between $X/h =$ 11.1 and 11.8 in Fig. 7b).

Some differences can be observed between the two plots. At first, looking at the streamlines, the center of the mean recirculating structure shifts slightly from $(X/h = 9.82,\ Y/h = -0.11)$ to $(X/h = 9.76,\ Y/h = -0.04)$ by having water in place of a solid wall. Secondly, defining absolute velocity fluctuation by $|\text{rms}| = \sqrt{\text{rms}_U^2 + \text{rms}_V^2}$, one may notice that the highest values appear at the cavity entrance and along the nozzle wall in both cases (Fig. 7). However, investigating the lower |rms| values, one can find a minimum near the center of the main mean recirculating structure by having Plexiglas in the cavity. On the contrary, such local minimum is not visible when water is present in the bottom of the cavity. The recirculation area appears to be globally less stable than with a solid wall.

This is probably due to the presence of waves imposing additional surface irregularities observed on the liquid interface during the parametric liquid accumulation investigation [55]. Therefore, although the mean flowfield does not seem to be strongly affected by the presence of the liquid interface, the velocity fluctuation pattern appears to be locally influenced by the waves of the water surface.

Numerical Simulation Conditions

The slag reduction in the SRM could be achieved, for example, by an intensive parametric study by means of numerical simulation. Nevertheless, the validation of both the methodology and the solver is mandatory. As a first step of the validation process, the previously shown experimental configuration is modeled numerically.

The simulations are performed with the CFD-ACE+ commercial solver using LES turbulence modeling. The computations are based on the experimental conditions. Accordingly, the numerical domain is three-dimensional with 200 mm spanwise dimension. The irrelevance of two-dimensional simulations was proven during a preliminary study [56]. As it is shown in Fig. 8, the geometry corresponds to one-half of the test section, up to the splitting plate (see Fig. 2b). Furthermore, the properties of room-temperature air are set to the fluid.

The inlet of the numerical domain is located at $X/h = -2.8$. For this boundary, a two-dimensional mean velocity distribution is created by using two experimental velocity profiles. The first profile is taken from the xy plane of the previous PIV experiments. The second profile is measured with PIV in a plane parallel to the splitting plate (xz) in the middle of the test section. Based on these measurements, the inlet velocity distribution is generated as shown in Fig. 9. The rms value of each velocity component is also measured experimentally. Even though this value is not entirely constant along the profiles, a constant typical value is defined in the numerical simulation: $\text{rms}_U = 0.3\ \text{m/s}$, $\text{rms}_V = 0.5\ \text{m/s}$, and $\text{rms}_W = 0.5\ \text{m/s}$. As a perturbation, a random fluctuation is applied, which does not involve spatial nor temporal correlation.

The applied numerical methods to discretize the equations are second order in time (Crank–Nicolson method) and second-order limited in space. The linear equations of velocity and pressure correction are solved with the algebraic multigrid numerical solver. The convergence criterion of the iterative unsteady solver is set to a minimum residual of 10^{-3} or a maximum of 20 iterations in each time step. The subgrid stress tensor is modeled with a dynamic version of the Smagorinsky model.

The grid must be generated to be fine enough to approximate the details of the flow, while trying to reduce the computational effort to reach a converged solution. For this purpose, a hybrid mesh is created (some enlargements are shown in Fig. 10): a structured grid near the solid walls and the inhibitor to approximate the high gradient

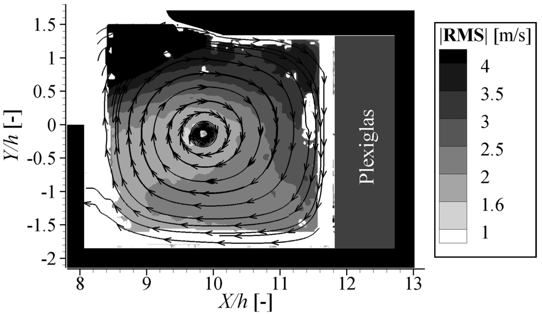

a) Plexiglass in the cavity (FoV #13)

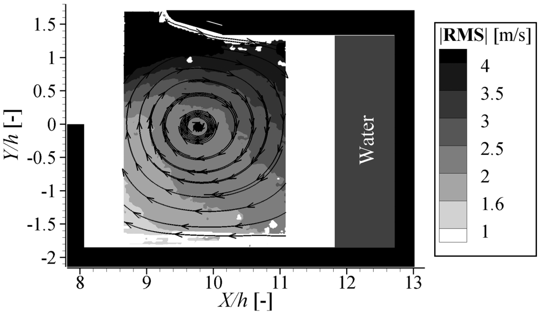

b) Water in the cavity

Fig. 7 Flowfield by changing the medium in the bottom of the cavity.

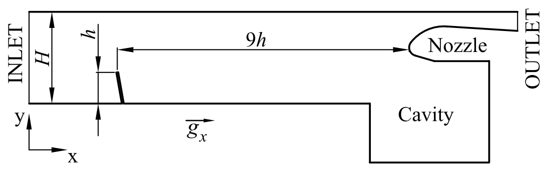

Fig. 8 Numerical domain geometry.

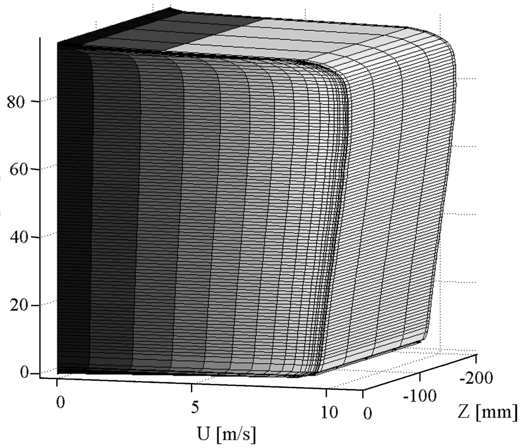

Fig. 9 Inlet velocity distribution.

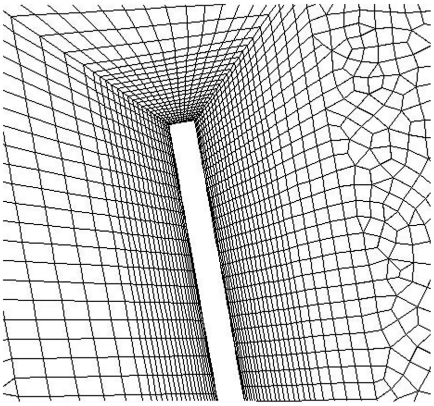

a) **At inhibitor**

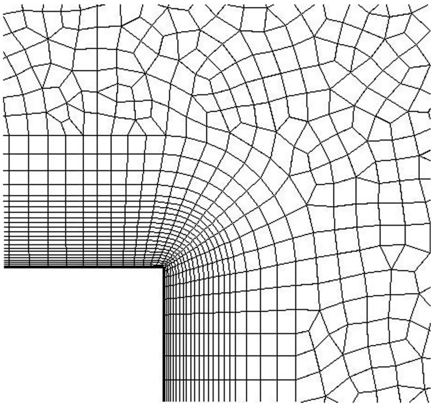

b) **Upstream the cavity corner**

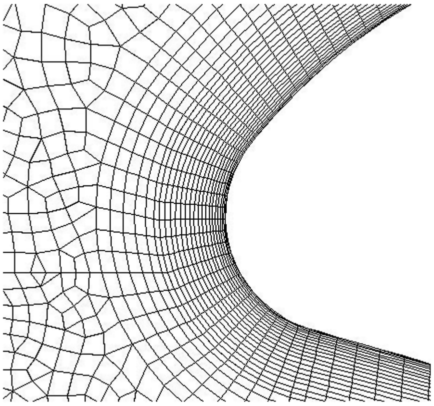

c) **At nozzle lip**

Fig. 10 Some examples of the hybrid grid of the numerical domain.

boundary layer and an unstructured quadrilateral mesh in the rest of the domain. The number of mesh points is 20786 × 50 (by having 50 cells in the z direction), which corresponds to about one million cells. The size of the smallest cell is as fine as $\Delta_{\min}/H = 4.25 \times 10^{-5}$. A time step of 2×10^{-5} s is used so as to keep a Courant–Friedrichs–Lewy condition of 0.425. This small time step has been chosen not for stability reasons, but to resolve the smallest time scale associated with the grid. During the simulation, the flowfield at every 60th time step is saved.

To resolve the boundary layer close to the walls, as was mentioned, a locally refined mesh is created. Thus, the $y+$ value remains below five on the bottom wall and on the cavity walls. On the lateral walls, this value rises up to 15 and, on the splitting plate and nozzle throat, $y+$ exceeds 20. In the near-wall regions when the laminar law (from viscous sublayer) cannot be resolved, the wall stress is modeled with the standard wall function.

A grid sensibility study was performed during which coarser and finer grids were employed (up to about 2 million total number of cells). As a result, the currently presented grid provided the optimal balance between computational resources and the best statistical validation with respect to the experimental data.

Validating the Numerical Data

To compare the unsteady numerical data to the statistical experimental results, 780 instantaneous fields are stored from the simulation during 18.72 flowthroughs (FTs) starting from the time step, where the flow is already established (about 2 FTs). One FT stands for the time required for a flow particle to travel through the computational domain at bulk velocity (presently, 1 FT $\cong 0.5\ \mathrm{m}/10\ \mathrm{m/s} = 0.05\ \mathrm{s}$). Later, from all the stored flowfields, the first- and second-order statistical moments are determined (mean and rms quantities). Finally, from the midspan plane of the 3-D numerical domain (defined by the laser-sheet position of the experiments), the in-plane components of the data are extracted and presented.

However, one should note that, although the experimental database is obtained from 1000 statistically independent samples (sampled at about 1 Hz) in each FoV, the 780 numerical samples (exported at a frequency of about 833 Hz, which is lower than the one associated with the time step) may be statistically correlated.

To investigate and illustrate this issue, the algorithm of Theunissen et al. [57] is applied on the computational fluid dynamics (CFD) fields. This statistical analysis tool based on moving block bootstrapping, determines the first- and second-order moments of a signal together with the errors of the momentum statistics at a given confidence level. Knowing the error, a rough estimate is given concerning the number of independent samples, which is to be evaluated in the present assessment. Currently, the local longitudinal velocity component U of the midspan plane data is assessed in each cell of the domain at a strict confidence level of 99%.

The resulting plot is shown in Fig. 11. As can be expected, the random inlet perturbation provides a good statistical independence. However, as the flow develops, the coherence gradually decreases the number of equivalent number of samples until the inhibitor. Downstream of the inhibitor, the statistical independence is marked by the local velocity magnitude and the turbulence quantities. Therefore, from the statistical point of view, the first part of the main recirculation bubble ($0 < X/h \leq 4$) and the rotating flow of the cavity are the most critical. These areas stand for even lower than 50 statistically independent samples. Therefore, here, the statistical quantities of the numerical simulation should be handled with care.

Despite the lower sample number for the low-velocity regions, it is still worthwhile to investigate the numerical flowfield, which is computationally very expensive. The high number of simulated flowthroughs should, however, allow us to report some general observations.

In Fig. 12, the distribution of the same quantities are shown as those presented in Fig. 6 related to the experimental study. Concerning the topology of the mean flowfields, the numerical field (Fig. 12a) resembles well the experimental data (Fig. 6a). The streamlines visualize the same mean circulating structures. Furthermore, the corresponding zones have similar sizes and positions.

The largest recirculating bubble extends from the inhibitor tip until the entrance of the cavity. Its center is located at ($X/h = 4.50$,

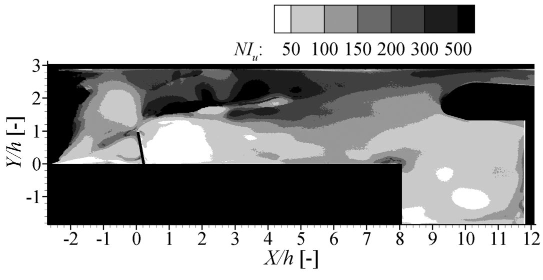

Fig. 11 Distribution of the equivalent number of statistically independent samples in the case of the numerical study.

$Y/h = 0.79$), which is about 10% more downstream and $0.10h$ closer (approximately 11%) to the sidewall than in the experiments. However, its height and therefore the dimension of the vena contracta of the freestream flow are very well reproduced (the total transversal dimension of the main bubble is only $0.05h$ larger numerically than experimentally).

In spite of the weak statistical convergence of the corresponding region, the mean flow rotation inside the cavity appears to be acceptable as well. The position of its center appears to be $0.05h$ closer to the nozzle transversely (it is located at $Y/h = -0.06$) and shifted $0.35h$ downstream longitudinally ($X/h = 10.17$). Its dimension is defined mainly by the three cavity walls and the nozzle. Therefore, no deviation is discovered here. However, one should note that the mean position of the center of this structure is not converged. As Fig. 13 shows, by changing even slightly the number of averaged samples, the center shifts considerably. Nevertheless, its deviation from the experimental values remains in an acceptable range.

Concerning the secondary circulating mean flow structures, they all appear in the time-averaged numerical results, even those that were not obtained entirely from PIV due to light reflection and optical access problems. Mostly, their location and dimension match very well with the experimental data.

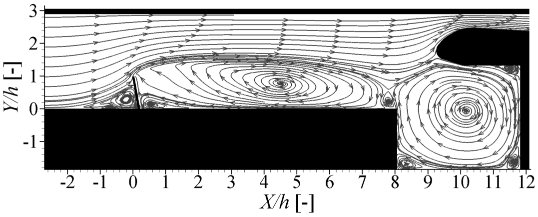

a) Streamlines of the mean flowfield

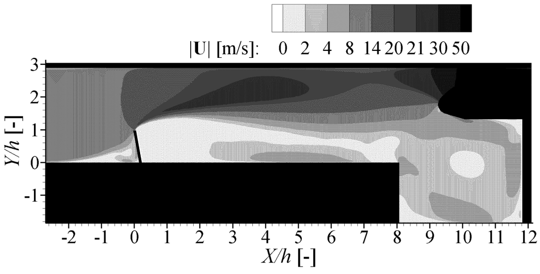

b) Mean velocity magnitude distribution

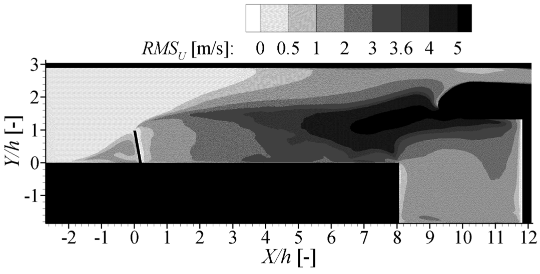

c) Fluctuation of the longitudinal velocity component

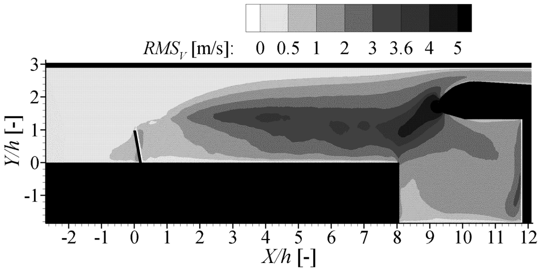

d) Fluctuation of the transversal velocity component

Fig. 12 Results of the time-averaged LES simulation in the symmetry plane (single-phase).

One of the aspects worth mentioning is the saddle point. This hyperbolic point [located at ($X/h = 7.78$, $Y/h = 0.65$) in the experiments] can be found at ($X/h = 7.79$, $Y/h = 0.56$) in the numerical plot. The saddle point is defined by the main recirculation bubble downstream of the inhibitor, the shear layer at the entrance of the cavity, the freestream flow, and the small mean circulating structure below it. If any of the mentioned structures were different, the saddle point would be displaced. As its longitudinal position matches remarkably well the experimental value, only the secondary circulating structure at the entrance corner of the cavity becomes slightly smaller transversely.

Finally, the smaller circulating structure at the downstream corner of the inhibitor shows slight differences with respect to the experimental results. First of all, its transversal dimension reduces from about $0.59h$ to $0.46h$. Consequently, the neighboring edge of the main recirculation bubble shifts locally closer to the sidewall.

As can be expected from the good agreement of the flow topology, globally the in-plane velocity magnitude plots (see Fig. 6b and 12b) also show very similar patterns and well-matching amplitudes. However, a more rapid flow acceleration can be seen in the vena contracta. Concentrating only on the local velocity maxima, although experimentally the 21 m/s value is reached farther downstream ($X/h > 2$), numerically this value appears already at $X/h < 1$.

In contrast, the upstream half of the main recirculation bubble ($X/h < 4$) represents lower velocity magnitudes numerically. This should be the consequence of the smaller secondary bubble and the slightly larger transversal main structure dimension. On the other hand, both in the downstream part of the same structure and in the cavity, well-matching velocity amplitudes can be found.

Concerning the velocity fluctuations (shown in Figs. 12c and 12d), the field should be divided again into two main regions: $X/h \leq 4.5$ and $X/h > 4.5$. In the first region (practically until the center of the main recirculating structure downstream the inhibitor), the standard deviation of both velocity components exhibit lower values than those that were observed during the experiments (shown in Figs. 6c and 6d). This underestimation probably originates from the definition of the random inlet turbulence, which represents neither spatial nor temporal correlation. However, in spite of the incorrect prediction until the region of the inhibitor, further downstream, a rather correct turbulence content is retrieved. As can be seen in the second zone, from $X/h > 4.5$, the levels of the fluctuation components are remarkably accurate. This observation is due to the natural unsteadiness of the shear layer attached to the inhibitor, which produces a shedding of coherent structures seeding the unsteady flowfield, which is captured accurately by the simulation.

To be able to compare more precisely the actual matching and deviation of the experimental and the numerical data, profiles of the longitudinal velocity component (U/U_0) and the velocity fluctuation magnitudes ($|\mathrm{rms}|/U_0$) are also extracted at four X/h positions (Figs. 14 and 15).

One profile is taken at $X/h = 0$, which corresponds to the tip of the inhibitor. The second profile is taken (according to the experimental

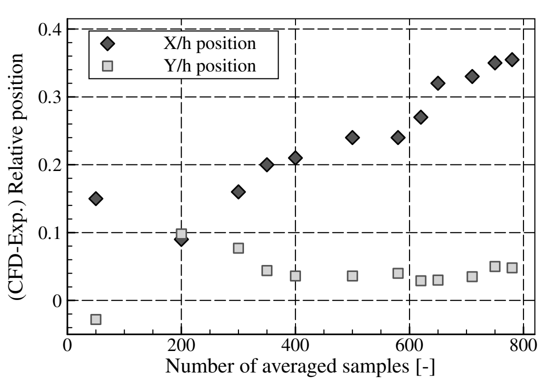

Fig. 13 Relative position of the center of the rotating structure of the cavity in function of the number of averaged samples (differences between the numerical positions and the experimental position used as reference).

data) approximately at the position of the center of the main mean recirculating structure ($X/h = 4$), which originates from the tip of the inhibitor and extends until the cavity. The third profile is desired to be extracted from the corner of the beginning of the cavity. However, in this region (due to the structure of the setup), the PIV measurements have locally low quality (see Fig. 6). Hence, the position of the third profile is defined slightly upstream, at $X/h = 7.6$. The fourth profile is defined at $X/h = 10$. This location is close to the center of the main mean swirling structure inside the cavity (according to the experimental data).

All the aforementioned observations derived from the contour plots can be seen locally more precisely in Figs. 14 and 15. Both the longitudinal velocity component and turbulence profiles depict a very good matching between the data sets. Therefore, even the statistical convergence of the CFD database at 18.72 FTs is considered to be sufficient.

As a summary, the extracted profiles and the contour plots show an acceptable agreement between the time-averaged numerical data and the ensemble-averaged experimental results, which proves the validity of the simulations and their applicability for further analysis in single-phase flow configuration.

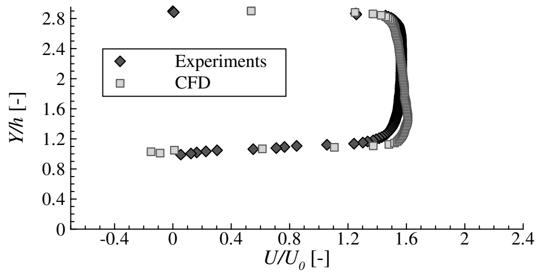

a) ***X/h* = 0*h***

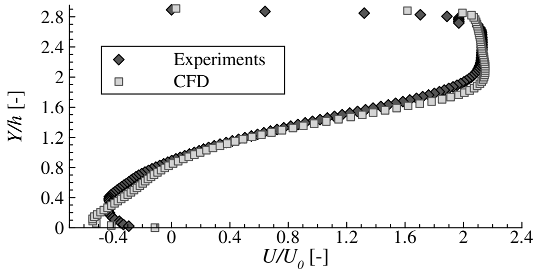

b) ***X/h* = 4*h***

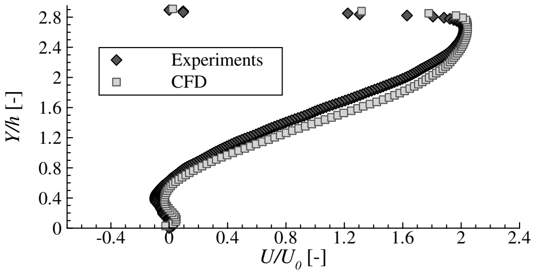

c) ***X/h* = 7.6*h***

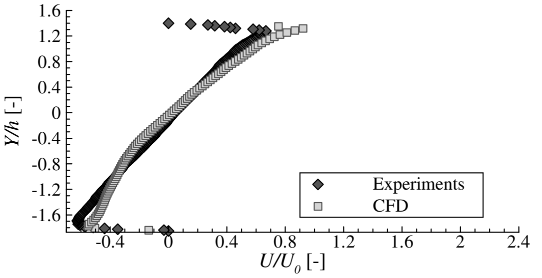

d) ***X/h* = 10*h***

Fig. 14 Midspan plane comparison between the experimental and the numerical longitudinal velocity components.

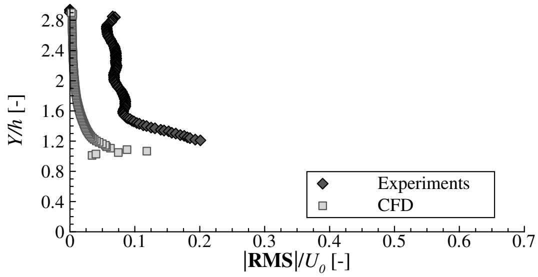

a) ***X/h* = 0*h***

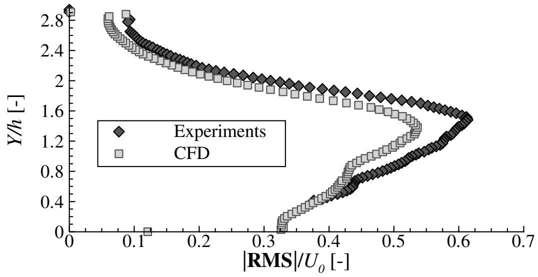

b) ***X/h* = 4*h***

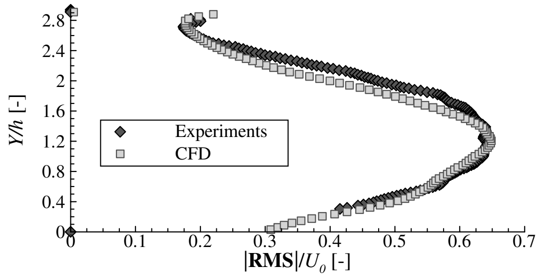

c) ***X/h* = 7.6*h***

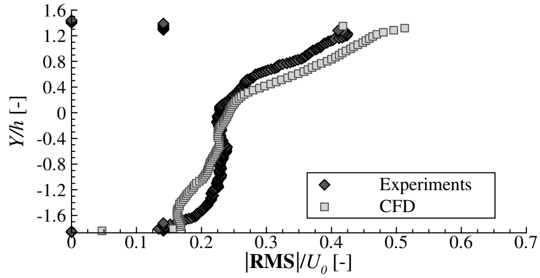

d) ***X/h* = 10*h***

Fig. 15 Midspan plane comparison between the experimental and the numerical velocity fluctuation magnitudes.

Wall Streamlines in Time-Averaged Flow

To have a more complete view of the topology of the time-averaged flow, the wall streamlines plotted on the lateral walls and on the bottom wall may be investigated. To do so, the velocity vectors used to draw the streamlines were measured at a distance of 10^{-2} mm from the wall.

The wall streamlines shown in Fig. 16 correspond to the side wall $Z = -2H$. To better describe this figure, a second one was created, Fig. 17a, where some characteristic points drawn by the wall streamline patterns are indicated with symbols. An explanation of the symbols can be seen in Fig. 18.

The circles with a light gray core correspond to sink points, where all the surrounding streamlines point toward the symbol. Once the flow particles arrive at these locations, they travel in the spanwise direction, moving away from the wall. There are two of them on the side wall and they govern the creation of the two main circulating regions of the flow: downstream of the inhibitor and inside the cavity.

Contrary to the sink points, there are the source points, which are represented by circles with a black core in Fig. 17. In this case, the wall streamlines escape from these points, and they are created by the flow that travels in the spanwise direction toward the wall. This occurs at seven locations on both side walls, created typically at the periphery of smaller recirculation regions of the flow and at the stagnation point near the nozzle tip.

As similar sink and source points appear on the $Z = 0$ wall (shown in Fig. 17b) at the same position, the corresponding locations can be considered to be the main points, where three-dimensionality is introduced in the recirculation zone. However, as these impingements are rather symmetric, a quasi-two-dimensional behavior is expected in the midspan plane. This behavior is confirmed by the plot corresponding to the bottom plane at $Y = 0$ (see Fig. 17c), where the streamlines are longitudinally oriented in the area of the midspan line ($Z/h = 2.99$).

Next, the convergence points are discussed, which are indicated by squares. These singular points are created by streamlines that travel on either side of the symbol in the opposite direction parallel to the walls. Such behavior can be observed at the detachment of the boundary layer upstream of the inhibitor. When they interact with each other, the resulting flow moves perpendicularly to the wall (see Fig. 18). These convergence points are located between counter-rotating flow structures. In the present case, they appear in the boundary between the main recirculation bubble centered in the cavity and the mean structures of the cavity corners. These points can also be found upstream and downstream of the inhibitor, where the mean secondary structures of the inhibitor corners interact with the main flow structures (on the upstream side of the detaching boundary layer, on the downstream side of the main recirculation).

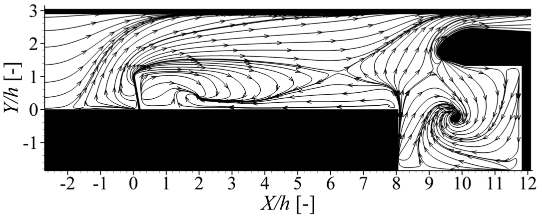

Fig. 16 Wall streamlines at the $Z = -200$ mm wall.

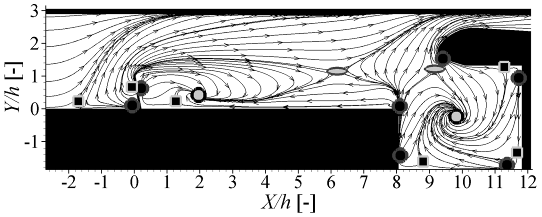

a) $Z = -200$ mm wall

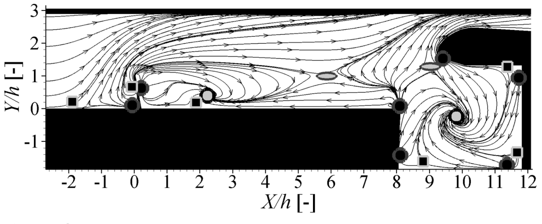

b) $Z = 0$ mm wall

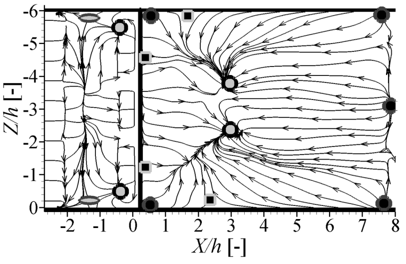

c) $Y = 0$ mm wall

Fig. 17 Wall streamlines and main flow features (the symbols are explained in Fig. 18).

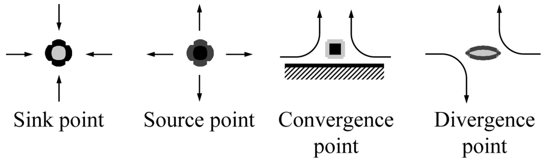

Fig. 18 Schematic of the highlighted flow features.

Finally, the elliptical spots represent the divergence points (saddle points), which are created by the boundaries of multiple flow structures.

Figure 17c shows the streamlines of the bottom wall. They were computed in the same way as the side wall, based on the in-plane velocity vectors at a distance of 10^{-2} mm. The plot reassures the symmetric flow behavior, which was observed at the lateral walls.

One should note that the sink point located at about $X/h \cong 2$ on the lateral walls, from where the streamlines are supposed to escape perpendicular to the wall, can be seen even by the pattern found on the bottom wall at the same location (around $X/h = 2$), represented by the convergence points. These streamlines supply the sink points located at about $Z/h = -2$ and $Z/h = -4$ (at about $X/h = 3$). The sink points indicate a major local rising flow from the bottom wall, which should contribute to the main recirculation bubble downstream of the inhibitor, which is driven by the freestream flow. However, the described pattern suggests that the part of the main recirculation bubble, which corresponds to higher Y/h values, transports the flow traces toward the lateral walls and therefore creates the three-dimensional behavior of the recirculation region closer to the lateral walls.

Conclusions

In the present paper, the first step of a long-term investigation related to the slag accumulation in a solid rocket motor model was presented. A cold-gas model has been constructed to reproduce characteristic elements of the real motor (inhibitor, nozzle, and cavity), which are assumed to be responsible for the generation of the driving forces of the slag accumulation phenomenon.

Detailed PIV experiments were performed in the midspan plane of the test section. From the experimental data, the main mean flow structures, the velocity magnitude, and the velocity fluctuations were presented.

Furthermore, experiments were carried out focusing on the nozzle cavity. The importance of having solid wall or liquid (simulating the slag) in the bottom of the cavity was investigated. It was shown that, by placing water into the cavity, the mean flow structure is slightly modified. However, the difference in the velocity fluctuation distribution is more important.

Representing the geometry and the boundary conditions of the experimental model, a 3-D large-eddy simulation was performed using a commercial solver (CFD-ACE+). The obtained time-averaged flow properties were successfully compared to the ensemble-averaged PIV database. The different recirculation zones as well as the unsteady vortex shedding were very well reproduced. This flowfield reproduction should be a sufficient basis to simulate a two-phase flow configuration and hence form the next step toward slag accumulation prediction. An experimental characterization of the two-phase flowfield in the same setup, including the interaction between the two phases, is already available for validation of the numerical prediction [58]. This experimental database took advantage of a newly developed two-phase particle image velocimetry method based on two excitation and two emission spectra to allow the two phases to be discriminated optically and simultaneously [59].

Finally, the wall streamlines were studied from the CFD results to show the mainly two-dimensional motion in the midspan plane and reveal the three-dimensional behavior of the mean flow structures.

Acknowledgment

This study has been supported by the ESA through the General Support Technology Programme activity number C51.MPA-818.

References

[1] Salita, M., "Predicted Slag Deposition Histories in Eight Solid Rocket Motors Using the CFD Model EVT," NATO Research and Technology Organization, Applied Vehicle Technology/von Karman Inst. Special Course *Internal Aerodynamics in Solid Rocket Propulsion*, edited by J. Anthoine and P. Kuentzmann, von Karman Inst., Rhode-Saint-Genèse, Belgium, May 2002.

[2] Beckstead, M. W., "A Model for Solid Propellant Combustion," *Proceedings of the 14th JANNAF Combustion Meeting*, Chemical Propulsion Information Agency Publ. 292, Vol. 1, 1977, p. 281.

[3] Cohen, N. S., "A Pocket Model for Aluminum Agglomeration in Composite Propellants," *AIAA Journal*, Vol. 21, No. 5, 1983, pp. 720–725.
doi:10.2514/3.8139

[4] Duterque, J., and Lambert, D., "Synthèse des Travaux sur l'agglomération de l'aluminium dans le Propergol du MPS P230," *Third Conference R&T CNES/ONERA Ecoulements Internes en Propulsion Solide*, Vol. 2, ONERA, Châtillon, France, March 1998, pp. 109–118.

[5] Jackson, T. L., Najjar, F., and Buckmaster, J., "New Aluminum Agglomeration Models and Their Use in Solid-Propellant-Rocket Simulations," *Journal of Propulsion and Power*, Vol. 21, No. 5, 2005, pp. 925–936.
doi:10.2514/1.11888

[6] Pevergne, T., and Le Helley, P., "Simulation Numérique des Impacts de Particules et du dépôt dans le MPS P230," *Third Conference R&T CNES/ONERA Ecoulements Internes en Propulsion Solide*, Vol. 2, ONERA, Châtillon, France, March 1998, pp. 201–210.

[7] Cesco, N., Dumas, L., Hulin, A., Pevergne, T., and Fabignon, Y., "Stochastic Models to the Investigation of Slag Accumulation in a Large Solid Rocket Motor," AIAA Paper 1997-3118, July 1997.

[8] Wirzberger, H., Macales, Y., and Yaniv, S., "Prediction of Slag Formation in a Solid Rocket Motor," AIAA Paper 2005-4488, July 2005.

[9] Godfroy, F., and Guéry, J.-F., "Unsteady Eulerian Flow Analysis of Solid Rocket Motor Slag," AIAA Paper 1997-2859, July 1997.

[10] Le Helley, P., Coste, S., and Pevergne, T., "Influence of the Unsteady Flow on the Alumina Flux Impinging the Nozzle and the Aft Dome of the Ariane 5 Booster," *Proceedings of the 2nd European Symposium on Launcher Technology, Space Solid Propulsion* [CD-ROM], Centre National d'Etudes Spatiales, Toulouse, France, Nov. 2000.

[11] Dupays, J., "Two-Phase Unsteady Flow in Solid Rocket Motors," *Aerospace Science and Technology*, Vol. 6, No. 6, 2002, pp. 413–422.
doi:10.1016/S1270-9638(02)01182-3

[12] Vuillot, F., "Vortex-Shedding Phenomena in Solid Rocket Motors," *Journal of Propulsion and Power*, Vol. 11, No. 4, 1995, pp. 626–639.
doi:10.2514/3.23888

[13] Traineau, J. C., Prevost, M., Vuillot, F., Le Breton, P., Cuny, J., Preioni, N., and Bec, R., "A Subscale Test Program to Assess the Vortex Shedding Driven Instabilities in Segmented Solid Motors," AIAA Paper 1997-3247, July 1997.

[14] Lupoglazo, N., and Vuillot, F., "Parietal Vortex Shedding as a Cause of Instability for Long Solid Propellant Motors. Numerical Simulations and Comparisons with Firing Tests," AIAA Paper 1996-0761, Jan. 1996.

[15] Vardelle, M., Escure, C., Fauchais, P., Platet, B., and Lavergne, G., "Impact of Alumina Droplets on Cold and Hot Surfaces," *Proceedings of the 2nd European Symposium on Launcher Technology, Space Solid Propulsion* [CD-ROM], Centre National d'Etudes Spatiales, Toulouse, France, Nov. 2000.

[16] Zaleski, S., and Gueyer, D., "Simulation de l'impact de Gouttes sur des Films Liquides," *Third Conference R&T CNES/ONERA Ecoulements Internes en Propulsion Solide*, Vol. 2, ONERA, Châtillon, France, March 1998, pp. 221–230.

[17] Meyer, R. X., "Coning Instability of Spacecraft During Periods of Thrust," *Journal of Spacecraft and Rockets*, Vol. 33, No. 6, 1996, pp. 781–788.
doi:10.2514/3.26838

[18] Dotson, K. W., Murdock, J. W., and Kamimoto, D. K., "Launch Vehicle Dynamic and Control Effects from Solid Rocket Motor Slag Ejection," *Journal of Propulsion and Power*, Vol. 15, No. 3, 1999, pp. 468–475.
doi:10.2514/2.5450

[19] Salita, M., "Deficiencies and Requirements in Modeling of Slag Generation in Solid Rocket Motors," *Journal of Propulsion and Power*, Vol. 11, No. 1, 1995, pp. 10–23.
doi:10.2514/3.23835

[20] Fabignon, Y., Guéry, J.-F., Godfroy, F., Le Helley, P., Hylkema, J., Jacques, L., Lavergne, G., and Villedieu, P., "Slag Accumulation in Large Segmented Solid Motors with a Submerged Nozzle," *Proceedings of the 2nd European Symposium on Launcher Technology, Space Solid Propulsion* [CD-ROM], Centre National d'Etudes Spatiales, Toulouse, France, Nov. 2000.

[21] Telara, M., Paglia, F., Stella, F., and Giangi, M., "Ariane 5 P230 SRM Frontal Thermal Protection Evolution: Numerical Simulation," AIAA Paper 2006-5242, July 2006.

[22] Najjar, F. M., Haselbacher, A., Balachandar, S., and Moser, R. D., "Simulations of Droplet Nozzle Impact and Slag Accumulation in the RSRM," AIAA Paper 2006-4588, July 2006.

[23] Fabignon, Y., Dupays, J., Avalon, G., Vuillot, F., Lupoglazo, N., Casalis, G., and Prevost, M., "Instabilities and Pressure Oscillations in Solid Rocket Motors," *Aerospace Science and Technology*, Vol. 7, No. 3, 2003, pp. 191–200.
doi:10.1016/S1270-9638(02)01194-X

[24] Tóth, B., Lema, M. R., Anthoine, J., and Steelant, J., "Assessment of Slag Accumulation in Solid Rocket Boosters: Summary of the VKI Research," AIAA Paper 2007-5760, July 2007.

[25] Culick, F. E. C., and Magiawala, K., "Excitation of Acoustic Modes in a Chamber by Vortex Shedding," *Journal of Sound and Vibration*, Vol. 64, No. 3, 1979, pp. 455–457.
doi:10.1016/0022-460X(79)90591-1

[26] Dunlap, R., and Brown, R. S., "Exploratory Experiments on Acoustic Oscillation Driven by Periodic Vortex Shedding," *AIAA Journal*, Vol. 19, No. 3, 1981, pp. 408–409.
doi:10.2514/3.7783

[27] Mettenleiter, M., Haile, E., and Candel, S., "Adaptive Control of Aeroacoustic Instabilities," *Journal of Sound and Vibration*, Vol. 230, No. 4, 2000, pp. 761–789.
doi:10.1006/jsvi.1999.2659

[28] Anthoine, J., Buchlin, J.-M., and Hirschberg, A., "Effect of Nozzle Cavity on Resonance in Large SRM: Theoretical Modeling," *Journal of Propulsion and Power*, Vol. 18, No. 2, 2002, pp. 304–311.
doi:10.2514/2.5935

[29] Guéry, J.-F., Avalon, G., Vuillot, F., Plourde, F., Anthoine, J., and Platet, B., "Use of Cold Flow Experiments in the ASSM Program: Lessons and Results," *Proceedings of the 2nd European Symposium on Launcher Technology, Space Solid Propulsion* [CD-ROM], Centre National d'Etudes Spatiales, Toulouse, France, Nov. 2000.

[30] Vetel, J., Plourde, F., Doan-Kim, S., and Prevost, M., "Cold Gas Simulation of the Influence of Inhibitor Shape in Combustor Combustion," *Journal of Propulsion and Power*, Vol. 21, No. 6, 2005, pp. 1098–1106.
doi:10.2514/1.7445

[31] Nguyen, C., Plourde, F., and Doan-Kim, S., "Analysis of Injecting Wall Inclination on Segmented Solid Rocket Motor Instability," *Journal of Propulsion and Power*, Vol. 24, No. 2, 2008, pp. 213–223.
doi:10.2514/1.29551

[32] Anthoine, J., and Lema, M., "Passive Control of Pressure Oscillations in Solid Rocket Motors: Cold-Flow Experiments," *Journal of Propulsion and Power*, Vol. 25, No. 3, 2009, pp. 792–800.
doi:10.2514/1.39794.

[33] Rael, M., Willert, C., and Kompenhans, J., *Particle Image Velocimetry: a Practical Guide*, Springer, New York, 1998.

[34] Anthoine, J., Mettenleiter, M., Repellin, O., Buchlin, J.-M., and Candel, S., "Influence of Adaptive Control on Vortex Driven Instabilities in a Scaled Model of Solid Propellant Motors," *Journal of Sound and Vibration*, Vol. 262, No. 5, May 2003, pp. 1009–1046.
doi:10.1016/S0022-460X(02)01034-9

[35] Piomelli, U., *Large-Eddy Simulation of Turbulent Flows: Introduction*, Lecture Series on Large Eddy Simulation and Related Techniques: Theory and Applications, von Karman Inst., Rhode-Saint-Genèse, Belgium, March 2006.

[36] Pope, S., *Turbulent Flows*, Cambridge Univ. Press, Cambridge, England, U.K., 2000.

[37] Smagorinsky, J., "General Circulation Experiments with the Primitive Equations, I: The Basic Experiment," *Monthly Weather Review*, Vol. 91, No. 3, 1963, pp. 99–164.
doi:10.1175/1520-0493(1963)091<0099:GCEWTP>2.3.CO;2

[38] Germano, M., Piomelli, U., Moin, P., and Cabot, W. H., "A Dynamic Subgrid-Scale Eddy Viscosity Model," *Physics of Fluids A*, Vol. 3, No. 7, 1991, pp. 1760–1765.
doi:10.1063/1.857955

[39] Beaudan, P., and Moin, P., "Numerical Experiments on the Flow past a

Circular Cylinder at Subcritical Reynolds Numbers," Dept. of Mechanical Engineering, Stanford Univ., TF-62, 1994.

[40] Brasseur, J. G., and Juneja, A., "Performance of Smagorinsky and Dynamic Models in near Surface Turbulence," *Div. of Fluid Dynamics Meeting*, American Physical Society, College Park, MD, Nov. 1997.

[41] Park, H.-J., "Direct and Large Eddy Simulation of Non-Equilibrium Wall-Bounded Turbulent Flows," *58th Annual Meeting of the Division of Fluid Dynamics*, American Physical Society, College Park, MD, Nov. 2005.

[42] Breuer, M., Jovii, N., and Mazaev, K., "Comparison of DES, RANS and LES for the Separated Flow Around a Flat Plate at High Incidence," *International Journal for Numerical Methods in Fluids*, Vol. 41, No. 4, 2003, pp. 357–388.
doi:10.1002/fld.445

[43] Kourta, A., "Shear Layer Instability and Acoustic Interaction in Solid Propellant Rocket Motors," *International Journal for Numerical Methods in Fluids*, Vol. 25, No. 8, 1997, pp. 973–981.
doi:10.1002/(SICI)1097-0363(19971030)25:8<973::AID-FLD599>3.0.CO;2-D

[44] Mombelli, C., Guichard, A., Godfroy, F., and Guéry, J.-F., "Parallel Computation of Vortex Shedding in Solid Rocket Motors," AIAA Paper 99-2510, 1999.

[45] Hulshoff, S. J., Hirschberg, A., and Hofmans, G. C. J., "Sound Production of Vortex Nozzle Interaction," *Journal of Fluid Mechanics*, Vol. 439, July 2001, pp. 335–352.

[46] Anthoine, J., Buchlin, J.-M., and Guéry, J.-F., "Effect of Nozzle Cavity on Resonance in Large SRM: Numerical Simulations," *Journal of Propulsion and Power*, Vol. 19, No. 3, 2003, pp. 374–384.
doi:10.2514/2.6141

[47] Cosyn, P., Vierendeels, J., and Anthoine, J., "Numerical Simulation of Aeroacoustic Phenomena in a Solid Rocket Booster," *Journal of Spacecraft and Rockets*, Vol. 42, No. 1, 2005, pp. 111–117.
doi:10.2514/1.3579.

[48] Apte, A., and Yang, V., "Unsteady Flow Evolution in Porous Chamber with Surface Mass Injection, Part 1: Free Oscillation," *AIAA Journal*, Vol. 39, No. 8, 2001, pp. 1577–1586.
doi:10.2514/2.1483

[49] Apte, A., and Yang, V., "Unsteady Flow Evolution in Porous Chamber with Surface Mass Injection, Part 2: Acoustic Excitation," *AIAA Journal*, Vol. 40, No. 2, 2002, pp. 244–253.
doi:10.2514/2.1666

[50] Apte, A., and Yang, V., "Large-Eddy Simulation Study of Transition and Flow Instability in a Porous-Walled Chamber with Mass Injection," *Journal of Fluid Mechanics*, Vol. 477, March 2003, pp. 215–225.

[51] Vetel, J., Plourde, F., Doan-Kim, S., and Guéry, J.-F., "Numerical Simulations of Wall and Shear-Layer Instabilities in Cold Flow Setup," *Journal of Propulsion and Power*, Vol. 19, No. 2, 2003, pp. 297–306.
doi:10.2514/2.6111

[52] Plourde, F., Najjar, F., Vetel, J., Wasistho, B., Doan-Kim, S., and Balachandar, S., "Numerical Simulations of Wall and Shear-Layer Instabilities in a Cold Flow Setup," AIAA Paper 2003-4674, July 2003.

[53] Scarano, F., "Particle Image Velocimetry Development and Application: Investigation of Coherent Structures in Turbulent Flows," Ph.D. Thesis, Univ. degli Studi di Napoli, Naples, Italy, March 2000.

[54] Scarano, F., and Riethmuller, M. L., "Advances in Iterative Multigrid PIV Image Processing," *Experiments in Fluids*, Vol. 29, No. 7, Dec. 2000, pp. S051–S060.
doi:10.1007/s003480070007

[55] Tóth, B., Lema, M. R., Anthoine, J., and Steelant, J., "Assessment of Slag Accumulation in Solid Rocket Boosters, Part II: Two-Phase Flow Experiments," AIAA Paper 2006-4430, July 2006.

[56] Lema, M. R., "Numerical Study of the Entrapment and Accumulation of Droplets in Solid Rocket Motors (SRM)," ESA Spanish Trainee Program Rept. ESA EWP-2275, Feb. 2005.

[57] Theunissen, R., Di Sante, A., Riethmuller, M. L., and Van den Braembussche, R. A., "Confidence Estimation Using Dependent Circular Block Bootstrapping: Application to the Statistical Analysis of PIV Measurements," *Experiments in Fluids*, Vol. 44, No. 4, 2008, pp. 591–596.
doi:10.1007/s00348-007-0418-8

[58] Tóth, B., Anthoine, J., and Steelant, J., "Experimental Characterization of a Two-Phase Flowfield in a Solid Rocket Motor Model," *Journal of Propulsion and Power*, Vol. 25, No. 4, 2009, pp. 914–920.
doi:10.2514/1.40599

[59] Tóth, B., Anthoine, J., and Riethmuller, M. L., "Two-Phase PIV Method Using Two Excitation and Two Emission Spectra," *Experiments in Fluids* [published online 23 May 2009].
doi:10.1007/s00348-009-0674-x

K. Frendi
Associate Editor